REPORT

2D MATERIALS

Out-of-equilibrium criticalities in graphene superlattices

Alexey I. Berdyugin[1,2]*†, Na Xin[1,2]†, Haoyang Gao[3], Sergey Slizovskiy[1,2], Zhiyu Dong[3], Shubhadeep Bhattacharjee[1,2], P. Kumaravadivel[1,2], Shuigang Xu[1,2], L. A. Ponomarenko[1,4], Matthew Holwill[1,2], D. A. Bandurin[1,2], Minsoo Kim[1,2]‡, Yang Cao[1,2], M. T. Greenaway[5,6], K. S. Novoselov[2], I. V. Grigorieva[1], K. Watanabe[7], T. Taniguchi[8], V. I. Fal'ko[1,2,9], L. S. Levitov[3], Roshan Krishna Kumar[1,2,10]*, A. K. Geim[1,2]*

In thermodynamic equilibrium, current in metallic systems is carried by electronic states near the Fermi energy, whereas the filled bands underneath contribute little to conduction. Here, we describe a very different regime in which carrier distribution in graphene and its superlattices is shifted so far from equilibrium that the filled bands start playing an essential role, leading to a critical-current behavior. The criticalities develop upon the velocity of electron flow reaching the Fermi velocity. Key signatures of the out-of-equilibrium state are current-voltage characteristics that resemble those of superconductors, sharp peaks in differential resistance, sign reversal of the Hall effect, and a marked anomaly caused by the Schwinger-like production of hot electron-hole plasma. The observed behavior is expected to be common to all graphene-based superlattices.

The electric response of metallic systems is routinely described by a Fermi surface displacement in momentum space, established through a balance between acceleration of charge carriers and their relaxation caused by scattering (*1*). The displacement is usually small, so that the drift velocity v_d is minute compared with the Fermi velocity v_F. In theory, if inelastic scattering is sufficiently weak, it should be possible to shift the Fermi surface so far from equilibrium that all charge carriers within the topmost, partially filled bands start streaming along the applied electric field E. The field would then start producing extra carriers through interband transitions (*2*), allowing electronic bands under the Fermi energy to contribute to the charge flow. Such an extreme out-of-equilibrium regime has never been achieved in metallic systems because Ohmic heating, phonon emission, and other mechanisms greatly limit v_d (*3–5*).

[1]School of Physics and Astronomy, University of Manchester, Manchester M13 9PL, UK. [2]National Graphene Institute, University of Manchester, Manchester M13 9PL, UK. [3]Massachusetts Institute of Technology, Cambridge, MA 02139, USA. [4]Department of Physics, University of Lancaster, Lancaster LA1 4YW, UK. [5]Department of Physics, Loughborough University, Loughborough LE11 3TU, UK. [6]School of Physics and Astronomy, University of Nottingham, Nottingham NG7 2RD, UK. [7]Research Center for Functional Materials, National Institute for Materials Science, 1-1 Namiki, Tsukuba 305-0044, Japan. [8]International Center for Materials Nanoarchitectonics, National Institute for Materials Science, 1-1 Namiki, Tsukuba 305-0044, Japan. [9]Henry Royce Institute for Advanced Materials, Manchester M13 9PL, UK. [10]Institut de Ciencies Fotoniques (ICFO), Barcelona Institute of Science and Technology, 08860 Castelldefels, Barcelona, Spain.
*Corresponding author. Email: alexey.berdyugin@manchester.ac.uk (A.I.B); roshankrishnakumar90@gmail.com (R.K.K.); geim@manchester.ac.uk (A.K.G.)
†These authors contributed equally to this work.
‡Present address: Department of Applied Physics, Kyung Hee University, Yong-In 17104, South Korea.

A rare exception is semimetallic graphene. At high carrier densities n, the drift velocity in graphene is limited by phonon emission (*6*, *7*), similar to other metallic systems. However, at low n, thermal excitations can create a relativistic plasma of massless electrons and holes, the "Dirac fluid." Its properties in thermodynamic equilibrium were in the focus of recent research (*8–12*), but the behavior at high biases represents an uncharted territory. Yet close to the Dirac point, even a small E can shift the entire Fermi surface and tap into a supply of carriers from another band (*13*, *14*). This can trigger processes analogous to the vacuum breakdown and Schwinger particle-antiparticle production in quantum electrodynamics, in which they are predicted to occur at enormous fields of ~10^{18} V m^{-1} (*15*). Because such E are inaccessible, it is enticing to mimic the Schwinger effect and access the resulting out-of-equilibrium plasma in a condensed matter experiment (*13*, *14*, *16*). Certain nonlinearities observed near graphene's neutrality point (NP) were previously attributed to the creation of electron-hole (e-h) pairs by means of a Schwinger-like mechanism (*13*, *14*), but the expected intrinsic behavior was obscured by low mobility, charge inhomogeneity, and self-gating effects (*6*, *17*).

We used graphene-based superlattices to identify an out-of-equilibrium state that sharply develops above a well-defined critical current j_c. The current marks an onset of the Schwinger pair production and a transition from a weakly dissipative fluid-like flow to a strongly dissipative e-h plasma regime. The out-of-equilibrium Dirac fluid is realized at surprisingly small E, thanks to the narrow electronic bands and low v_F characteristic of graphene superlattices (*18*, *19*). The resulting dual-band transport leads to striking anomalies in longitudinal and Hall resistivities. Counterintuitively, an apparent drift velocity in this regime exceeds v_F. With hindsight, we show that the current-induced critical state can be reached even in standard graphene, by using extra-high currents allowed by the point contact geometry.

The studied superlattices were of two types: graphene crystallographically aligned on top of hexagonal boron nitride (G/hBN) (*20–23*) and small-angle twisted bilayer graphene (TBG) (*24–28*). The superlattices were encapsulated in hBN, to ensure high electronic quality, and shaped into multiterminal Hall bar devices by using the standard fabrication procedures (*29*). The devices were first characterized by measuring their longitudinal resistivity ρ as a function of n as shown in Fig. 1, A to C, for three representative devices. The twist angles θ were determined from measurements of Brown-Zak oscillations (*30*); for TBG, θ was intentionally chosen away from the magic angle to avoid many-body states (*27*, *28*). Aside from the familiar peak in ρ at zero doping, satellite peaks indicating secondary NPs were observed at n that agreed well with the θ values (*20–22*, *26*). For G/hBN superlattices, the low-energy electronic spectrum is practically identical to that of monolayer graphene (*18*), and the spectral reconstruction occurs only near and above the edge of the first miniband (Fig. 1D, top). By contrast, all minibands in TBG are strongly reconstructed (Fig. 1D, bottom) (*19*). At low biases (Fig. 1, A to C, and fig. S1), our devices exhibited transport characteristics similar to those reported previously for G/hBN and TBG superlattices (*20–22*, *26*).

Next, we studied high-bias transport using current densities j up to 0.1 mA μm^{-1}, limited only to avoid device damage. Unless stated otherwise, all the reported measurements were carried out at the bath temperature T = 2 K. The superlattices exhibited qualitatively similar current-voltage (*I-V*) characteristics (Fig. 1, E to G), which were nearly linear at $j <$ 0.01 mA μm^{-1} and then rapidly switched into a high-resistance state so that the differential resistivity dV/dI showed a pronounced peak at a certain critical current j_c. The behavior was universal, found in all our devices (more than 10) (figs. S3 and S6), if the Fermi energy was tuned inside narrow minibands (that is, away from the main NP in the case of G/hBN). The *I-V* characteristics in Fig. 1, E to G, strongly resemble the superconducting response, despite electron transport being ballistic at low j and viscous at moderate currents (*31*); ρ always remained finite, although could be as low as <0.01 kilohms, a few orders of magnitude smaller than dV/dI above j_c. Further details are provided in Fig. 2 by showing dV/dI as a function of n, where the narrow white arcs indicate peaks in dV/dI. Considerable similarities

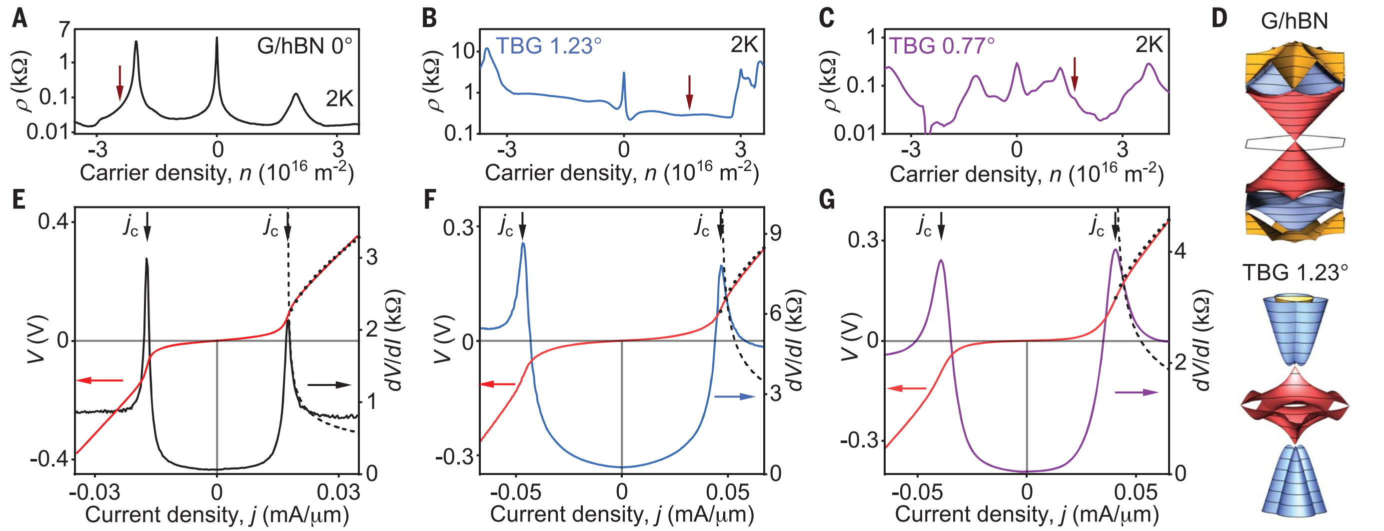

Fig. 1. Linear and nonlinear transport in graphene superlattices. (**A** to **C**) ρ(*n*) in the linear regime (j = 50 nA μm^{-1}) for (A) G/hBN with θ ≈ 0° and for TBG with (B) θ ≈ 1.23° and (C) θ ≈ 0.77°. Micrographs of the studied devices are provided in (*29*). (**D**) Band structures of G/hBN and TBG 1.23° superlattices (*29*). Colors indicate different energy bands. The bands are shown for the energy range of ±340 and ±80 meV for G/hBN and TBG 1.23°, respectively. (**E** to **G**) *I-V* characteristics for the devices in panels (A) to (C), respectively. The doping levels for the curves are indicated with the arrows in (A) to (C). The dependence $(j - j_c) \propto V^{3/2}$ expected above j_c is indicated by the dotted curves and the corresponding $dV/dI \propto (j - j_c)^{-1/3}$ is indicated by the dashed curves. All *V* and *dV/dI* are normalized according to devices' aspect ratios.

are clearly seen across different superlattice types. One feature shared by all the maps was the rapidly decreasing j_c as n approached NPs (Fig. 2, A to C, and figs. S2 and S6). The only exception was the main NP in G/hBN superlattices, where the resistivity in its vicinity increased monotonically for all accessible j (fig. S2).

To gain more insight, we studied the Hall effect in small (nonquantizing) magnetic fields B. An example of such measurements for G/hBN near the hole-side NP is shown in Fig. 2D. At small j, the Hall voltage V_{xy} increased linearly with j, and dV_{xy}/dI was positive, reflecting the hole doping. However, dV_{xy}/dI abruptly turned negative above j_c, revealing a change in the dominant-carrier type. dV_{xy}/dI maps for the G/hBN and TBG superlattices are shown in Fig. 2, E to G. There are clear correlations between the longitudinal and Hall maps so that the peaks in dV/dI and the Hall effect's reversal occurred at same j_c. The observed nonlinearities were robust against T up to ~50 K, above which the peaks in dV/dI became gradually smeared (fig. S4). This shows that Ohmic heating—which is generally expected at high j (*14*, *31*, *32*)—was not the reason for the critical-current behavior (*29*).

The rapid decrease in j_c near all secondary NPs prompts the question why such a critical-current behavior was not observed in graphene (*13*, *14*) or near the main NP of G/hBN (Fig. 2A) and whether it can be achieved at some higher j. With this in mind, we used a point contact geometry that funneled the current through a short constriction, whereas wide adjacent regions provided a thermal bath for electron cooling. This allowed us to reach j an order of magnitude greater than those achievable in the standard geometry. At these j, *I-V* characteristics near the main NP of G/hBN superlattices became similar to those near its secondary NPs (fig. S3), although they were more smeared because of Ohmic heating and, possibly, edge irregularities in the superlattice periodicity within narrow constrictions. To circumvent the latter problems and demonstrate the universality of the critical behavior at all NPs, we made constrictions from nonsuperlatticed graphene (monolayer graphene encapsulated in hBN but nonaligned). These devices also displayed a clear critical behavior, although peaks at j_c were notably broader because of heating (Fig. 3A).

To understand the criticalities, we first discuss the conceptually simplest case of the Dirac spectrum, such as in nonsuperlatticed graphene. We consistently observed that the transition between the low- and high-resistance states occurred at $j_c \approx nev_F$ (e is the electron charge)—that is, at $v_d \approx v_F$, independently of n (Fig. 3B). This condition means that the Fermi surface is shifted from equilibrium by the entire Fermi momentum, and all electrons in the conduction band move along E with a drift velocity of about v_F (Fig. 3C). If the spectrum were fully gapped, j could not increase any further because all available carriers already move at maximum speed. This should result in saturation of j as a function of V, which is in agreement with the observations at $j \lesssim j_c$. Simulations of this intraband-only transport corroborate our conclusions (Fig. 3A, dashed curves). To explain the supercritical behavior at $j > j_c$, for a gapless spectrum E can move electrons up in energy from the valence band into the conduction band, leaving empty states (holes) behind (Fig. 3C, bottom). The extra electrons and holes created by the interband transitions allow the current to exceed j_c. Accordingly, the apparent $v_d = j/ne$ seemingly exceeds the maximum possible group velocity, v_F (because n is fixed by gate voltage, but the actual concentration of carriers increases by Δn). Quantitatively, the e-h production at $j > j_c$ can be described by the Schwinger (or Zener-Klein tunneling) mechanism. It can generate interband carriers at a rate $\propto E^{3/2}$ (*13*, *16*), but at small biases, the production is forbidden by the Pauli exclusion principle. Above j_c, the Fermi distribution is shifted sufficiently far from equilibrium so that E depletes the states near the NP, which eliminates the Pauli blocking and enables the e-h pair production (Fig. 3C). Accounting for e-h annihilation (recombination processes bring the electronic system back into the equilibrium), we found the stationary concentration of extra carriers Δn to be $\propto E^{3/2} \propto V^{3/2}$, if $\Delta n \ll n$ (*29*). This translates into extra current $\Delta nev_F \propto V^{3/2}$ and $dV/dI \propto j^{-1/3}$. Because dV/dI decreases for $j > j_c$ but increases for $j < j_c$, a peak is expected at j_c, which is in agreement with Fig. 3A.

The above analysis can also be applied to graphene superlattices. Their narrow minibands display low v_F, and therefore, the onset of interband transitions is expected at small j. The switching transition in our superlattices occurred at v_d typically >10 times smaller than in nonsuperlatticed graphene (fig. S5). This yields a characteristic v_F of several 10^4 m s^{-1}, which translates into minibands' widths

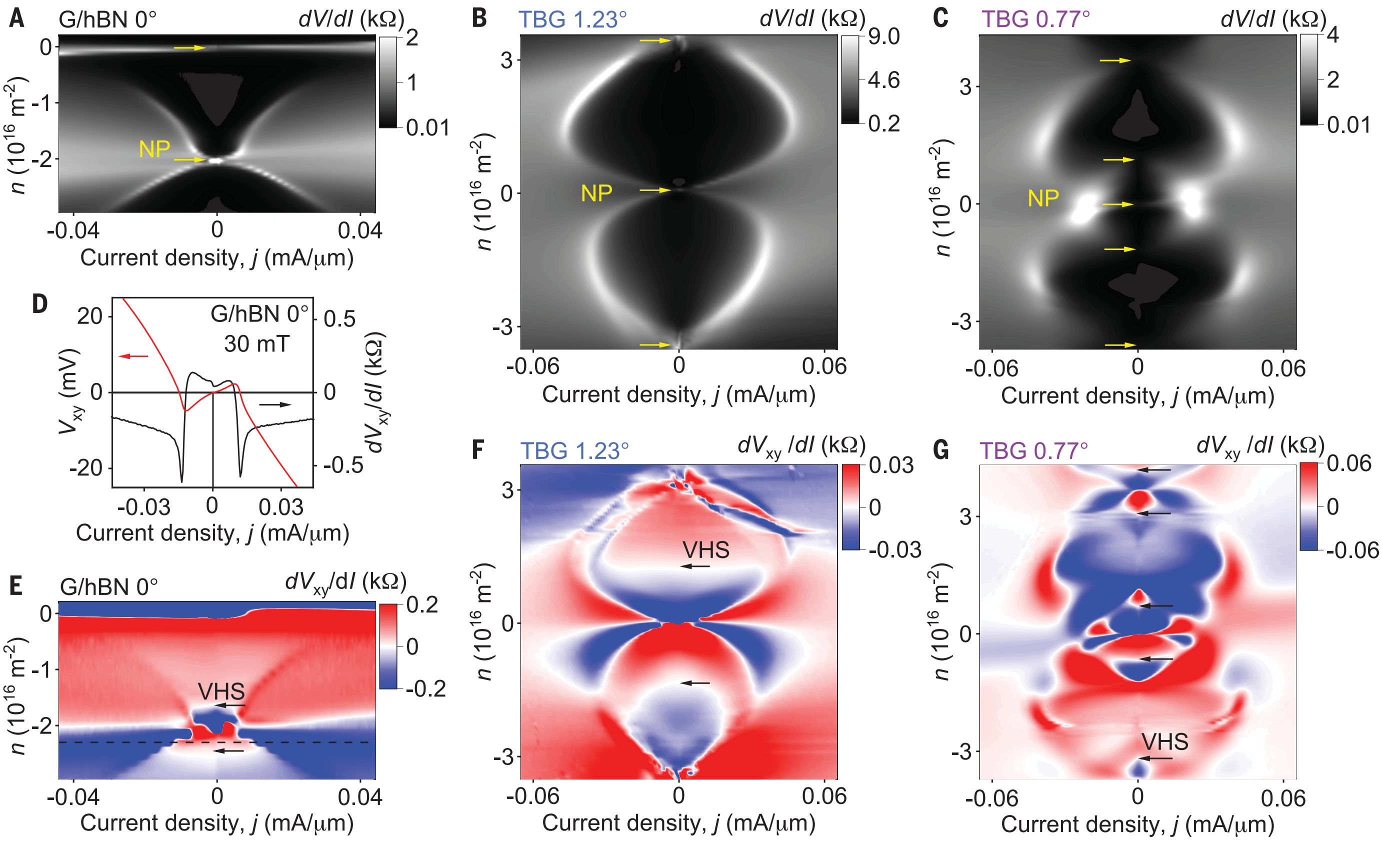

Fig. 2. Switching into the high-bias regime. (**A** to **C**) dV/dI as a function of j and n for the superlattices in Fig. 1, A, to C, respectively. Bright arcs appear at the critical current. Yellow arrows indicate NPs as found with low-bias measurements (*29*). (**D**) Hall voltage (red curve) and the corresponding differential resistivity (black curve) measured at n indicated by the dashed line in (E). (**E** to **G**) Maps of dV_{xy}/dI for the superlattices in (A) to (C), respectively. B = 30 mT; T = 2 K. The black arrows indicate positions of van Hove singularities.

of ~10 meV, as expected from band structure calculations (*19*). For the relatively small j_c, superlattices were much less affected by heating than graphene and, accordingly, exhibited sharper transitions (Figs. 2 and 3A). The experimental *I-V* curves are compared with the above predictions for Schwinger-like carrier generation in Fig. 1, E to G. Good agreement was found for $j \gtrsim j_c$. Notable deviations seen at highest j are expected because Δn is no longer small compared with n, the assumption used to derive the plotted dependences (*29*). Furthermore, j_c in graphene evolved $\propto n$ as expected for the Dirac spectrum (Fig. 3B). By contrast, superlattices exhibited clear deviations from the linear dependence (Figs. 2, A to C). This is attributed to the group velocity of charge carriers rapidly decreasing away from secondary NPs, dropping to zero at van Hove singularities (VHSs). If nonequilibrium carriers reside near VHSs, they move at low speed and contribute little to the current (fig. S5C), leading to the sublinear $j_c(n)$, as observed experimentally.

Extending the described physics onto the Hall effect, it is straightforward to understand the sign changes in Fig. 2, D to G. With reference to Fig. 3C, interband transitions result in extra holes near the NP plus extra electrons that effectively appear at higher energies in the out-of-equilibrium Fermi distribution (Fig. 3C). For superlattices, contributions of these e-h pairs into V_{xy} do not cancel each other because of the broken e-h symmetry, which results in different masses and mobilities of the extra carriers. The effect is particularly strong upon approaching a VHS. For example, if the dominant carriers are electrons, their distribution would be shifted by E upward toward a VHS (fig. S5C), and they should have heavy masses. By contrast, the reciprocal holes generated near the NP should be light (fig. S5C). These higher-mobility holes are expected to provide a dominant contribution into the Hall signal, and therefore, dV_{xy}/dI should change its sign from electron to hole near $j \approx j_c$, as observed experimentally. If the asymmetry is sufficiently strong, even V_{xy} can reverse its sign (Fig. 2D). The observed changes in the Hall effect can qualitatively be described by using the two-carrier model with different mobilities of out-of-equilibrium electrons and holes (fig. S7).

Last, we discuss the interband carrier generation at the main NP in graphene (Fig. 3), which closely mimics the Schwinger effect in quantum electrodynamics. Consequences of the Schwinger-like effect at the Dirac point are qualitatively different from those described by Zener-Klein tunneling at finite doping (*29*). In contrast to the latter case, there is no low-to-high resistance switching at n = 0, and dV/dI rapidly drops with increasing j, reaches a minimum, and then gradually increases (Fig. 3D). This behavior was highly reproducible for all graphene constrictions (fig. S8) but, because of self-gating and heating effects, could not be observed in the standard geometry, where *I-V* curves were similar to those in the literature (*6*). The initial drop is attributed to e-h puddles present at NPs, in which small E starts generating interband carriers along puddles' boundaries and enhances conductivity (*13*). Minima in dV/dI typically occurred at $j_m \approx 0.05$ mA μm^{-1} (Fig. 3D), which translates into $\Delta n = j_m/ev_F \approx 3 \times 10^{10}$ cm^{-2}, which is in agreement with the charge inhomogeneity δ found in our devices. In principle, the initial dV/dI drop could be fitted again by $\propto j^{-1/3}$, but such fits were inconclusive because of the involved inhomogeneity. For higher j so that $\Delta n \gg \delta$, the Schwinger production fills graphene with a plasma of electrons and holes in equal concentrations, $n_e \approx n_h = \Delta n$. Because

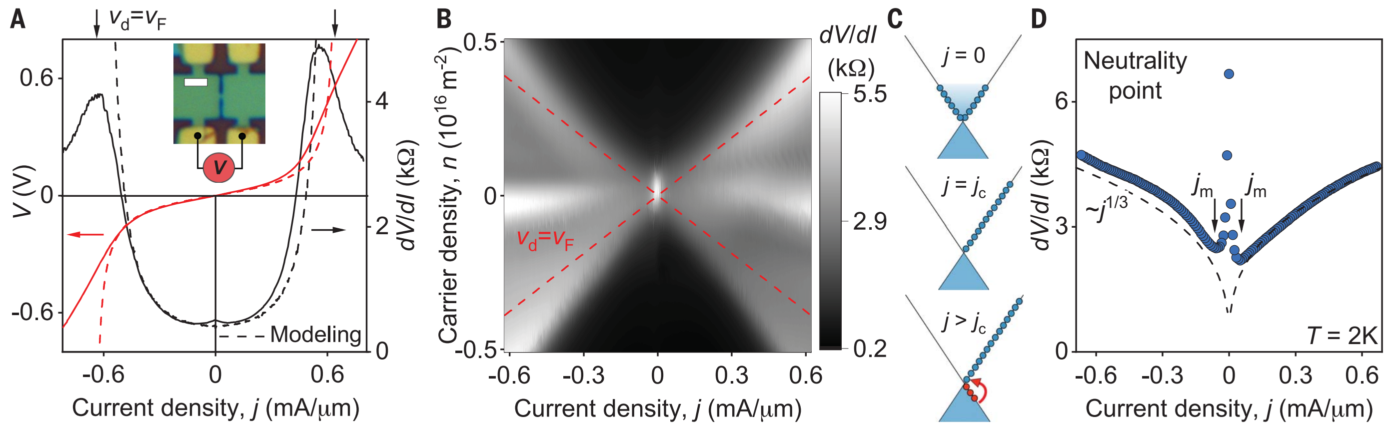

Fig. 3. Nonlinear transport in nonsuperlatticed graphene near the Dirac point. (**A**) Voltage and differential resistance (red and black curves, respectively) for a constriction of 0.4 μm in width; $n = 0.4 \times 10^{16}$ m^{-2}. (Inset) Optical micrograph of the graphene device and its measurement geometry. Scale bar, 2 μm. The small bump at zero bias is caused by electron-electron scattering (*34*). Dashed curves indicate *I-V* characteristics calculated for the Dirac spectrum at $j < j_c$ (*29*). The vertical arrows indicate j with $v_d = v_F = 1 \times 10^6$ m s^{-1}. (**B**) Example of dV/dI maps for graphene constrictions. Red lines indicate $j = nev_F$. (**C**) Schematic of graphene's spectrum and its occupancy in (top) equilibrium and in out-of-equilibrium for (middle) $j = j_c = nev_F$ and for (bottom) $j > j_c$. Blue and red circles indicate electrons and holes, respectively. The red arrow illustrates e-h pair production. (**D**) dV/dI at the NP for a 0.6-μm-wide constriction. The arrows indicate minima.

the annihilation rate of e-h pairs scales with $n_e n_h = \Delta n^2$, theory predicts (*29*) that the Schwinger production rate ($\propto E^{3/2}$) leads to $\Delta n \propto E^{3/4}$, resulting in $dV/dI \propto j^{+1/3}$. This contrasts the reported Zener-Klein behavior at graphene's NP (*13*) but is in quantitative agreement with our experiment (Fig. 3D and fig. S8). For highest j, the hot e-h plasma inside graphene constrictions is expected to approach the quantum critical limit (*8*–*12*), in which e-h scattering is governed by the uncertainty principle and ρ is predicted to become rather universal, ~$1.3\alpha^2(h/e^2)$, where α is the interaction constant and h/e^2 is the resistance quantum (*8*, *9*). For encapsulated graphene, $\alpha \approx 0.3$, whereas the constriction geometry results in resistance of ~1.8ρ (*29*). Accordingly, the quantum-critical resistance for our constrictions is expected to be ~5 kilohms, which is in qualitative agreement with Fig. 3D and fig. S8, where the curves approach this value. We do not expect better agreement because E strongly disturbs the e-h plasma, making it anisotropic, which is rather different from the Dirac fluids in thermal equilibrium, which were discussed previously (*8*–*12*). This anisotropic regime requires further theoretical analysis and would be interesting to probe through other experimental techniques.

At high biases, Fermi liquids in graphene-based systems can be turned into Dirac-like fluids characterized by intense interband carrier generation. The transition between the weakly and strongly dissipative electronic states is marked by peculiar superconducting-like dV/dI. Such *I-V* characteristics, although of interest on their own right as a signature of out-of-equilibrium criticalities, also serve as a warning that they alone—without other essential attributes (such as zero resistance)—do not constitute a proof of "emerging/fragile" superconductivity. It is possible that the nonlinear response reported in some graphene-based flat-band systems [for example, (*33*)] was governed by the out-of-equilibrium physics rather than superconductivity. Other attributes of nonequilibrium behavior such as Bloch oscillations and associated terahertz radiation are likely to accompany the reported criticalities, which is an appealing opportunity for further investigation.

REFERENCES AND NOTES

1. C. Kittel, *Introduction to Solid State Physics* (Wiley, ed. 8, 2005).
2. C. Zener, *Proc. R. Soc. A Math. Phys. Eng. Sci.* **145**, 523–529 (1934).
3. W. Shockley, *Bell Syst. Tech. J.* **30**, 1035–1037 (1951).
4. E. J. Ryder, *Phys. Rev.* **90**, 766–769 (1953).
5. S. M. Sze, K. K. Ng, *Physics of Semiconductor Devices* (Wiley-Interscience, 2007).
6. I. Meric *et al.*, *Nat. Nanotechnol.* **3**, 654–659 (2008).
7. M. A. Yamoah, W. Yang, E. Pop, D. Goldhaber-Gordon, *ACS Nano* **11**, 9914–9919 (2017).
8. L. Fritz, J. Schmalian, M. Müller, S. Sachdev, *Phys. Rev. B Condens. Matter Mater. Phys.* **78**, 085416 (2008).
9. A. B. Kashuba, *Phys. Rev. B Condens. Matter Mater. Phys.* **78**, 085415 (2008).
10. J. Crossno *et al.*, *Science* **351**, 1058–1061 (2016).
11. P. Gallagher *et al.*, *Science* **364**, 158–162 (2019).
12. M. J. H. Ku *et al.*, *Nature* **583**, 537–541 (2020).
13. N. Vandecasteele, A. Barreiro, M. Lazzeri, A. Bachtold, F. Mauri, *Phys. Rev. B Condens. Matter Mater. Phys.* **82**, 045416 (2010).
14. W. Yang *et al.*, *Nat. Nanotechnol.* **13**, 47–52 (2018).
15. J. Schwinger, *Phys. Rev.* **82**, 664–679 (1951).
16. D. Allor, T. D. Cohen, D. A. McGady, *Phys. Rev. D Part. Fields Gravit. Cosmol.* **78**, 096009 (2008).
17. Y. Wu *et al.*, *ACS Nano* **6**, 2610–2616 (2012).
18. J. R. Wallbank, A. A. Patel, M. Mucha-Kruczynski, A. K. Geim, V. I. Fal'ko, *Phys. Rev. B Condens. Matter Mater. Phys.* **87**, 245408 (2013).
19. R. Bistritzer, A. H. MacDonald, *Proc. Natl. Acad. Sci. U.S.A.* **108**, 12233–12237 (2011).
20. L. A. Ponomarenko *et al.*, *Nature* **497**, 594–597 (2013).
21. C. R. Dean *et al.*, *Nature* **497**, 598–602 (2013).
22. B. Hunt *et al.*, *Science* **340**, 1427–1430 (2013).
23. M. Yankowitz, Q. Ma, P. Jarillo-Herrero, B. J. LeRoy, *Nat. Rev. Phys.* **1**, 112–125 (2019).
24. Y. Cao *et al.*, *Phys. Rev. Lett.* **117**, 116804 (2016).
25. K. Kim *et al.*, *Proc. Natl. Acad. Sci. U.S.A.* **114**, 3364–3369 (2017).
26. Y. Cao *et al.*, *Nature* **556**, 80–84 (2018).
27. L. Balents, C. R. Dean, D. K. Efetov, A. F. Young, *Nat. Phys.* **16**, 725–733 (2020).
28. E. Y. Andrei, A. H. MacDonald, *Nat. Mater.* **19**, 1265–1275 (2020).
29. Materials and methods are available in the supplementary materials.
30. R. Krishna Kumar *et al.*, *Science* **357**, 181–184 (2017).
31. D. A. Bandurin *et al.*, *Science* **351**, 1055–1058 (2016).
32. M. Freitag *et al.*, *Nano Lett.* **9**, 1883–1888 (2009).
33. S. Xu *et al.*, *Nat. Phys.* **17**, 619–626 (2021).
34. E. S. Tikhonov *et al.*, *Phys. Rev. B Condens. Matter Mater. Phys.* **90**, 161405 (2014).
35. A. I. Berdyugin *et al.*, Out-of-equilibrium criticalities in graphene superlattices. *Zenodo* (2021); doi:10.5281/zenodo.5639021.

ACKNOWLEDGMENTS

Funding: We acknowledge financial support from the European Research Agency (grants ARTIMATTER and VANDER), Lloyd's Register Foundation, Graphene Flagship Core3 Project, and the Royal Society. M.T.G acknowledges the support from EPSRC grant EP/V008110/1, and A.I.B. acknowledges the support from NOWNANO Doctoral Training Centre. R.K.K. acknowledges a ESPRC doctoral-prize fellowship award and the EU Horizon 2020 program under the Marie Skłodowska-Curie grants 754510 and 893030. V.I.F. was also supported by EU Quantum Flagship Project 2D-SIPC and EPSRC grants EP/V007033 and EP/S030719. L.L. acknowledges support from the Science and Technology Center for Integrated Quantum Materials, NSF grant DMR-1231319, and Army Research Office grant W911NF-18-1-0116. K.W. and T.T. acknowledge support from Elemental Strategy Initiative of Japan (grant JPMXP0112101001) and JSPS KAKENHI (19H05790, 20H00354, and 21H05233). L.S.L. acknowledges support by the Science and Technology Center for Integrated Quantum Materials, NSF grant DMR-1231319, and Army Research Office grant W911NF-18-1-0116. **Author contributions:** A.I.B., R.K.K., and A.K.G. conceived and led the project; N.X., P.K., S.X., M.H., and Y.C. made the studied devices; A.I.B., S.B., L.A.P., D.A.B., M.K., and R.K.K. carried out the measurements and analyzed their results, with help from N.X., S.S, P.K., K.S.N., I.V.G., L.S.L., V.I.F., and A.K.G.; H.G., S.S., Z.D., M.T.G., A.I.B., V.I.F., and L.S.L. provided theory; K.W. and T.T. supplied hBN crystals. A.I.B., R.K.K., and A.K.G. wrote the manuscript, with contributions from L.S.L., N.X., H.G., S.S., and I.V.G. All authors discussed the results and commented on the manuscript. **Competing interests:** The authors declare no competing interests. **Data and materials availability:** All data discussed in the main text and the supplementary materials are available at Zenodo (*35*).

SUPPLEMENTARY MATERIALS

science.org/doi/10.1126/science.abi8627
Supplementary Text
Figs. S1 to S8
References (*36*–*46*)

7 April 2021; accepted 16 December 2021
10.1126/science.abi8627

Science

Out-of-equilibrium criticalities in graphene superlattices

Alexey I. BerdyuginNa XinHaoyang GaoSergey SlizovskiyZhiyu DongShubhadeep BhattacharjeeP. KumaravadivelShuigang XuL. A. PonomarenkoMatthew HolwillD. A. BandurinMinsoo KimYang CaoM. T. GreenawayK. S. NovoselovI. V. GrigorievaK. WatanabeT. TaniguchiV. I. Fal'koL. S. LevitovRoshan Krishna KumarA. K. Geim

Science, 375 (6579), • DOI: 10.1126/science.abi8627

Displacing the Fermi surface
Electrons that contribute to electrical conduction in a metal typically occupy high energy levels near the Fermi level. To get electrons from lower bands to join the flow, extremely large electric fields would be needed. In graphene and its superlattices, Berdyugin *et al*. show that small, experimentally accessible fields are sufficient to achieve this regime. The researchers discerned the signatures of this highly nonequilibrium state in transport data. —JS